UNIVERSITY OF CALIFORNIA,
IRVINE

Control of the Hydrogen Evolution Reaction on Metal Oxides for Energy Storage

DISSERTATION

submitted in partial satisfaction of the requirements
for the degree of

DOCTOR OF PHILOSOPHY

in Materials Science and Engineering

by

William Gaieck

Dissertation Committee:
Professor Shane Ardo, Chair
Professor Daniel Mumm
Professor Zuzanna Siwy

2019

DEDICATION

To

My parents, Guadalupe and Raymond, who have worked hard to provide their children with the opportunities, experiences, & higher quality of life that they themselves never had.

My siblings, Grace, Omar, and Raymond Jr.

All my friends, but especially:
Michele A. Ivañez, Joyce Lin, Joe M. Schlegel,
Evelyn Valdez-Ward, Connie Tran, & Albert Blattler.

All my generous neighboring labs that assisted me on various occasions:
Law Lab, Corn Lab, Yang Lab, Penner Lab, Borovik Lab, Mumm Lab, and Guan Lab.

Thank you to Professors Noona Bakhiet, Jonathan Atwater, and David Brown for believing in, encouraging, and empowering me.

My labmates past and present.

Most importantly, Dane W. Samilo, PhD, who has been an amazing, compassionate, and supportive partner in the rollercoasters that are graduate school and life.

I <4 you
(because four is greater than three)

It takes a village to raise a child.

TABLE OF CONTENTS

LIST OF FIGURES

LIST OF TABLES

ACKNOWLEDGMENTS

I would like to thank my committee chair, Professor Shane Ardo, who helped me to become an expert in electrochemistry and took me on as a budding graduate student many years ago. For instilling in me, to think “on my toes” while experimenting and to critically scrutinize data and its analysis.

I would like to thank my committee members, Professor Daniel Mumm and Professor Zuzanna Siwy, for providing insight, guidance, and thoughtful questions that promoted growth in my work.

A thank you to Drs. Dmitry Fishman and Mingjie Xu, who helped me with spectroscopy and microscopy; respectively. Both are seriously underrated despite their major contributions across UC Irvine.

Thank you to my wonderful undergraduate researchers that I had the privilege to mentor: Anni Zhang, Nancy Estrada, John Hylak, Sabeena Sebastian, and Jerry Siu.

Finally, I would like to thank Zejie Chen for graciously and expeditiously assisting me with experiments towards the end of my time at UC Irvine and after.

CURRICULUM VITAE

William "Iam" Gaieck

2011 B.S. in Chemistry, University of California, San Diego

2015 M.S. in Materials Science and Engineering, University of California, Irvine

2019 Ph.D. in Materials Science and Engineering, University of California, Irvine

FIELD OF STUDY

(Photo)electrochemistry, (Spectro)electrochemistry, and Materials Characterization Related to Energy Conversion and Energy Storage

PUBLICATIONS

Gaieck, W.; Ardo, S. Challenges and Opportunities for Ion-Exchange Membranes in Solar Fuels Devices. *Rev. Adv. Sci. Eng.* **2014**, *4* (4), 1–11. https://doi.org/10.1166/rase.2014.1075.

ABSTRACT OF THE DISSERTATION

Control of the Hydrogen Evolution Reaction on Metal Oxides for Energy Storage

By

William Gaieck

Doctor of Philosophy in Materials Science & Engineering

University of California, Irvine, 2019

Professor Shane Ardo, Chair

Hydrogen can be used as a replacement for fossil fuels in many applications. However, commercially relevant scales of hydrogen production utilize either electrolysis or a combination of steam methane reforming and the water gas shift reaction which are energy intensive and non-renewable. Here I report on a portion of work toward understanding the fundamental physical and chemical phenomena that constrain the maximum solar-to-hydrogen (STH) conversion efficiency for photoelectrochemical particle-slurry reactors. Using Rh-doped strontium titanate (SrTiO 3 :Rh), a variable power light source, and an inline-mass spectrometry the rate of hydrogen production can be controlled and optimized.

In the second part of my work, I report on the spectro-electrochemical behavior of crystalline titanium dioxide (TiO_2) mesoporous films as a model system for aqueous redox flow battery charging/discharging. The effects of potential determining ions on the density of states in the materials are discussed.

INTRODUCTION

Photoelectrochemical (PEC) water electrolysis, colloquially referred to as solar water splitting, may one day provide a renewable supply and storage of energy, in the form of molecular hydrogen (H_2), propelling the world toward a global hydrogen-fueled economy. While a hydrogen economy is likely decades or more away, PEC research is a highly active community in pursuit of the "Holy Grail" of water splitting.[1] The "Holy Grail" being photocatalyst(s), i.e. semiconductor materials, with the proper band gap, band alignment, and corrosion stability that are capable of both long-life cycle and high efficiency solar-to-hydrogen production.

As will be discussed in greater detail later, the state-of-the-art in the PEC field is divided into two general reactor form factors. One form factor consists of particle-based systems and the other of a monolithic-like electrode(s). Within each of the form factors are two prototypical reactors, those composed of particles are termed either **type-I** or **type-II**, and the monolithic-like electrodes are either **type-III** or **type-IV**. The monolithic-like reactors are the more mature of the technologies with research dominated by **type-III** reactors. Generally, these reactors suffer from high fabrication, processing and materials costs. Such systems frequently utilizing copper indium gallium selenide (CIGS) photocatalysts can achieve solar-to-hydrogen (STH) efficiencies over 10%.[2–4] Despite the high efficiency, this family of reactors still have significant barriers, including poor reactor operating lifetime and cycling due to (photo)corrosion. While much of the PEC research has focused on the monolithic-based technologies, comparatively little research has been conducted on the particle-based technologies. Therefore, these **type-I/II** reactors and more generally the technologies associated with them are immature. Such systems have had STH efficiencies reported as high as 5%, for a single particle in suspension and up to 1.1% for Z-scheme sheets in suspension.[5–7] However, the circumstances under which these STH values have

been obtained are questionable in light of unreported H_2/O_2 production rates, unsustainable cycling procedures, and a general lack of verification and replication by other groups. Thus, the currently accepted and replicable state-of-the-art for particle-based STH efficiencies are approximately 0.1% using a doped strontium titanate or strontium titanate/bismuth vanadate pairs.[8,9] Thus, there exists ample room for STH efficiency growth in **type-I/II** systems.

Based on a detailed techno-economic analysis of photoelectrochemical hydrogen production, the four prototypical PEC reactors were investigated to determine the cost of producing hydrogen fuel.[10] The study forecasted that **type-II** reactor systems could be made at a fraction of the cost of **type-III/IV** systems and at a hydrogen production price point which could be competitive with gasoline. Several assumptions were made about these systems with respect to cost, materials, and efficiency with great uncertainty. Further, as these particle-based reactors are immature, a lot of unknowns about these reactors remain, including details of the nano-particle material system, the amount of piping needed to circulate the system, optimal reactor dimensions/geometry, and their longevity; among many other things. These unknowns coupled with no standards for experimental methods and protocols for testing particle-based PEC systems are areas ripe for investigation.

Chapter 1

A brief primer on photoelectrochemistry for PEC reactors

Broadly, in plants photosynthesis uses water, carbon dioxide, and light to produce carbohydrates and oxygen. The process converts energy, as light from the sun, to energy stored in the form of chemical bonds (carbohydrates). Similarly, the solar fuels community seeks to use the energy, as light from the sun, to convert precursor materials, i.e. CO_2 and water, into economically valuable and fuels on the industrial scale, like hydrogen and simple hydrocarbons.[11] The former fuel is less complex to make from water than the latter is to make from carbon dioxide- owing to lower bond activation energies and lower overpotentials; the focus of the research herein is concerned with production of hydrogen from water.[12] Despite nearly a half-century since the first photoelectrochemical experiments in 1972 by Fujishima and Honda, much of this field remains under active study.[1,13]

In photoelectrochemical (PEC) water electrolysis, colloquially referred to as water-splitting, the production of hydrogen from water proceeds as follows: light (i.e. photons) with energy greater than or equal to the bandgap (E_g) of a semiconductor (photocatalyst) material generates an electron-hole pair (**Equation 1.1**).

$$E_{h\nu \geq E_g} \rightarrow e^-(electron) + h^+(hole) \quad (1.1)$$

If the hole has enough energy it may than go on to oxidize water, this is termed the oxygen evolution reaction (OER). The oxidation half-reaction for water is given by

$$2H_2O(l) \rightarrow O_2(g) + 4H^+ + 4e^- \quad (1.2)$$

If the electron has sufficient energy it may than go on to reduce hydrogen ions (or hydroniums), this is termed the hydrogen evolution reaction (HER). The reduction half-reaction for water is given by

$$2H^+ + 2e^- \rightarrow H_2\,(g) \tag{1.3}$$

Thus, the overall reaction for water splitting produces both hydrogen and oxygen in a 2:1 ratio and is given by

$$2H_2O \rightarrow 2H_2 + O_2 \tag{1.4}$$

The overall reaction (**Equation 1.4**) and sequence of events are for the idealized case when there are no side reactions occurring and when an appropriate single material is capable of overall water splitting. Furthermore, a material must also have the following bandgap structure, beyond an appropriately sized band gap, the material's conduction band (CB) must lie more negative than the standard reduction potential for the water reduction half-reaction and the valence band must lie more positive than the standard reduction potential for the water oxidation half-reaction. Only a relatively small group of materials possess the bandgap structure requirements for water splitting. Moreover, materials possessing the needed band structure may lack suitability in other critical areas which make long-lived materials for hydrogen production generally difficult to achieve. To accommodate deficiencies in any one photocatalyst material, such as with incorrect band alignment, two photocatalysts can be utilized with a redox mediator to overcome such barriers in a so-called Z-scheme configuration.[14] In this configuration, redox shuttles in solution mediate charge between particles in solution, such that each half of the water splitting reaction occurs only on one of the two types of particles along with a redox shuttle regenerative process. In the case of the HER occurring on a particle, that same particle will use its generated hole to oxidize the shuttle, as in

$$D + h^{+}(hole) \rightarrow A \quad (1.5)$$

Where, *D*, is a donor species capable of donating an electron to the hole in the semiconductor, and *A*, is now the oxidized, electron acceptor form of the shuttle. Similarly, in the case of the OER occurring at the other type of particle, that particle will use its generated electron to reduce the shuttle, as in

$$A + e^{-}(electron) \rightarrow D \quad (1.6)$$

Thus, the redox mediator allows the combination of two photocatalyst materials that would otherwise be unsuitable for overall water splitting.

Beyond knowledge of the basics of water splitting, the physical device configuration (PDC), for the purposes of real industrial scale hydrogen production, determines the parameter space within which the researcher can operate. Thus, it is important to understand water splitting research in the context of its intended PDC, for which there are a few. There are two general schemes for PDC in photoelectrochemical water splitting with each having two prototypical types of reactors associated with it. One scheme of reactors is particle-based. While the other scheme is considered to be a monolithic electrode or wafer-based. Each scheme, as well as the reactors associated with it, have their own associated parameter spaces.[10,15]

The most researched of the schemes are of the monolithic electrode variety. These systems are composed of a photovoltaic (i.e. photocatalyst) submerged in solution where photogenerated carriers are directly used in electrolysis. This configuration is known as a type-III reactor. Similarly, a type-IV system has the addition of a solar concentrator. Both reactors benefit from compartmentalization of each half-reaction (i.e. O_2 and H_2) thereby avoiding potentially explosive mixtures of the gases. Moreover, the systems can be operated at sufficiently high pressures to avoid pressurizing product gasses at a later stage. However, both

reactors suffer from costly fabrication, processing, use of precious metals (e.g. Pt, Ru, and Ir), and poor long-term stability. Despite these issues monolithic electrode reactors remain some of the most well studied physical device configurations for photoelectrochemical water electrolysis.

The second general scheme for PDC of photoelectrochemical water splitting reactors are particle-based. These systems utilize particles in solution, in the Z-scheme, to generate H_2 and O_2. When the particles are confined to a single compartment, both half-reactions as well as product gases are in close proximity to one another; the reactor is termed type-I. Alternatively, when each half-reaction is compartmentalized in a particle-based system the reactor is termed type-II. In type-I systems, the explosive limits for hydrogen and oxygen mixing are an inherent issue along with required separation of the gases at a later stage. Whereas, in type-II systems each half-reaction is in a separate compartment and crossover of the products is prevented by use of a semipermeable membrane, which only allows for electronic and ionic conduction across compartments.[16] Based upon a US Department of Energy commissioned technoeconomic analysis, these particle-based technologies have been predicted to be cost-competitive with fossil fuels on a gallons of gas equivalent basis.[10] Despite the appeal of cost-competitive solar fuels, the particle-based family of technologies remain immature as compared to their wafer-based counter parts and the accuracy of their H_2 production costs rely heavily upon a poorly understood operation and parameter space. Thus, they require further investigation relative to wafer-based technologies.

In order to better understand the operation and parameter space of the type-II reactor systems, investigation into each part of the system with respect to physical and chemical properties, and dominant or governing phenomena is needed. Broadly, areas of interest where a

better understanding would be helpful are in the photocatalyst materials, the co-catalysts and deposition methods used, redox shuttles, and photoelectrochemical methods of investigation.

Many of the PEC photocatalyst materials, i.e. semiconductors, with bandgaps amenable to water electrolysis may be synthesized using one or more of the following techniques: sol-gel, solvo-thermal, and solid state synthesis. In particular, sol-gel and solvo-thermal techniques have the potential to be used for both preparation of inks for stationary electrodes and free-floating particles in solution. Moreover, for a variety of these materials these methods of synthesis allow fine control over the bandgap, particle size, shape, dispersity, crystallinity, phase, and texture among other materials properties.[17–19] These properties may be interrogated via diffuse reflectance spectroscopy, to determine the bandgap; scanning electron microscopy, to determine particle size, shape, and dispersity; and x-ray crystallography, to determine phase and crystallinity. Since many of these properties have varying effects on PEC performance, control of material properties is necessary to obtain high performance materials and high efficiency PEC systems.

Despite favorable materials properties for PEC electrolysis, in order to overcome kinetic barriers, photocatalysts have often require the use of co-catalysts which lower the activation barriers of the relevant reactions (**Equations 1.2** and **1.3**). Typically, noble or binary metals, like platinum, are used for facile production of hydrogen, in the water reduction half-reaction. Whereas, metal oxides, are typically used to facilitate production of oxygen, in the water oxidation half-reaction. Deposition of these catalysts onto photocatalysts generally relies on one of three techniques, either electroless- or electro- or photoelectro- deposition. For photocatalyst materials that will be used as free-floating particles in solution, photoelectrodeposition- has been the preferred method of electrocatalyst deposition.[20]

While much focus is on the solid materials used, i.e. the semiconductors and catalysts, the effects of redox mediators in solution have received less attention. Redox shuttles in solution are needed to mediate charge within and across compartments in the reactor, for these z-scheme systems. While a large variety of redox couples are known and well-studied in other electrochemical experimental contexts, those relating to use in PEC reactors require further understanding of the physical and chemical property space related to their effects on overall device performance and efficiency. Knowing the physical properties of the redox shuttles such as absorbance spectra, solubility, and diffusion coefficient can provide information on competitive absorption of light, whether or not the redox shuttle will be solvated at an arbitrary concentration and can be used to predict the spatiotemporal concentration profile of the shuttle in the reactor. Whereas, knowing the chemical properties and more generally interactions between shuttle-catalyst or shuttle-semiconductor, such as adsorptive properties, exchange current density, overpotential, and behavior of shuttle at varying pH- can provide information on competitive adsorption/inhibition of species, asymmetry in redox chemistry of shuttles, redox shuttle kinetics, and chemical reactivity of species (e.g. proton-coupled electron transfer). These properties of redox shuttles may be interrogated using standard electrochemistry techniques (e.g. cyclic voltammetry, potential-step experiments), for kinetic and thermodynamic behavior; and ultra violet-visible (UV-Vis) spectroscopy, for kinetic information and species concentration. The parameter space for redox shuttles in PEC systems is complex and highly interdependent, as are the components of the system, perhaps that is why it remains a relatively poorly charted area of research.

References

(1) Bard, A.; Fox, M. A. Artificial Photosynthesis: Solar Splitting of Water to Hydrogen and Oxygen. *Acc. Chem. Res.* **1995**, *28*, 141–145 DOI: 10.1021/ar00051a007.

(2) Jacobsson, T. J.; Fjällström, V.; Sahlberg, M.; Edoff, M.; Edvinsson, T. A Monolithic Device for Solar Water Splitting Based on Series Interconnected Thin Film Absorbers Reaching over 10% Solar-to-Hydrogen Efficiency. *Energy Environ. Sci.* **2013**, *6* (12), 3676 DOI: 10.1039/c3ee42519c.

(3) Juodkazyt??, J.; Seniutinas, G.; ??ebeka, B.; Savickaja, I.; Malinauskas, T.; Badokas, K.; Juodkazis, K.; Juodkazis, S. Solar Water Splitting: Efficiency Discussion. *Int. J. Hydrogen Energy* **2016**, *41* (28), 11941–11948 DOI: 10.1016/j.ijhydene.2016.05.079.

(4) Khaselev, O.; Bansal, A.; Turner, J. A. High-Efficiency Integrated Multijunction Photovoltaic/electrolysis Systems for Hydrogen Production. *Int. J. Hydrogen Energy* **2001**, *26* (2), 127–132 DOI: 10.1016/S0360-3199(00)00039-2.

(5) Liao, L.; Zhang, Q.; Su, Z.; Zhao, Z.; Wang, Y.; Li, Y.; Lu, X.; Wei, D.; Feng, G.; Yu, Q.; Cai, X.; Zhao, J.; Ren, Z.; Fang, H.; Robles-Hernandez, F.; Baldelli, S.; Bao, J. Efficient Solar Water-Splitting Using a Nanocrystalline CoO Photocatalyst. *Nat. Nanotechnol.* **2014**, *9* (1), 69–73 DOI: 10.1038/nnano.2013.272.

(6) Liu, J.; H.; Liu, Y.; Zhong, J.; Li, Y.; Zhang, S.; Kang, Z. Water Splitting. Metal-Free Efficient Photocatalyst for Stable Visible Water Splitting via a Two-Electron Pathway. *Science* **2015**, *347* (6225), 970–974 DOI: 10.1126/science.aaa3145.

(7) Wang, Q.; Hisatomi, T.; Jia, Q.; Tokudome, H.; Zhong, M.; Wang, C.; Pan, Z.; Takata, T.; Nakabayashi, M.; Shibata, N.; Li, Y.; Sharp, I. D.; Kudo, A.; Yamada, T.; Domen, K. Scalable Water Splitting on Particulate Photocatalyst Sheets with a Solar-to-Hydrogen Energy Conversion Efficiency Exceeding 1%. *Nat. Mater.* **2016**, *15* (March), 1–3 DOI: 10.1038/nmat4589.

(8) Kato, H.; Sasaki, Y.; Shirakura, N.; Kudo, A. Synthesis of Highly Active Rhodium-Doped SrTiO3 Powders in Z-Scheme Systems for Visible-Light-Driven

Photocatalytic Overall Water Splitting. *J. Mater. Chem. A* **2013**, *1* (39), 12327 DOI: 10.1039/c3ta12803b.

(9) Asai, R.; Nemoto, H.; Jia, Q.; Saito, K.; Iwase, A.; Kudo, A. A Visible Light Responsive Rhodium and Antimony-Codoped SrTiO3 Powdered Photocatalyst Loaded with an IrO2 Cocatalyst for Solar Water Splitting. *Chem. Commun. (Camb).* **2014**, *50* (19), 2543–2546 DOI: 10.1039/c3cc49279f.

(10) James, B. D.; Baum, G. N.; Perez, J.; Baum, K. N. Technoeconomic Analysis of Photoelectrochemical (PEC) Hydrogen Production. *DOE Contract Number GS-10F-009J* **2009**, *22201* (December), 1–128.

(11) Smith, W. A.; Sharp, I. D.; Strandwitz, N. C.; Bisquert, J. Interfacial Band-Edge Energetics for Solar Fuels Production. *Energy Environ. Sci.* **2015**, *8* (October 2015), 2851–2862 DOI: 10.1039/C5EE01822F.

(12) Montoya, J. H.; Seitz, L. C.; Chakthranont, P.; Vojvodic, A.; Jaramillo, T. F.; Nørskov, J. K. Materials for Solar Fuels and Chemicals. *Nat. Mater.* **2017**, *16* (1), Page# to be added DOI: 10.1038/nmat4778.

(13) Fujishima, A.; Honda, K. Electrochemical Photolysis of Water at a Semiconductor Electrode. *Nature* **1972**, *238*, 37–38.

(14) Maeda, K. Photocatalytic Water Splitting Using Semiconductor Particles: History and Recent Developments. *J. Photochem. Photobiol. C Photochem. Rev.* **2011**, *12* (4), 237–268 DOI: 10.1016/j.jphotochemrev.2011.07.001.

(15) Xiang, C.; Weber, A. Z.; Ardo, S.; Berger, A.; Chen, Y.; Coridan, R.; Fountaine, K. T.; Haussener, S.; Hu, S.; Liu, R.; Lewis, N. S.; Modestino, M. A.; Shaner, M. M.; Singh, M. R.; Stevens, J. C.; Sun, K.; Walczak, K. Modeling, Simulation, and Implementation of Solar-Driven Water-Splitting Devices. *Angew. Chemie Int. Ed.* **2016**, 2–17 DOI: 10.1002/anie.201510463.

(16) Gaieck, W.; Ardo, S. Challenges and Opportunities for Ion-Exchange Membranes in Solar Fuels Devices. *Rev. Adv. Sci. Eng.* **2014**, *4* (4), 1–11 DOI: 10.1166/rase.2014.1075.

(17) Schneider, J.; Matsuoka, M.; Takeuchi, M.; Zhang, J.; Horiuchi, Y.; Anpo, M.; Bahnemann, D. W. Understanding TiO 2 Photocatalysis : Mechanisms and Materials. *Chem. Rev.* **2014**, *114*, 9919–9986 DOI: 10.1021/cr5001892.

(18) Nair, V.; Perkins, C. L.; Lin, Q.; Law, M. Textured Nanoporous Mo:$BiVO_4$ Photoanodes with High Charge Transport and Charge Transfer Quantum Efficiencies for Oxygen Evolution. *Energy Environ. Sci.* **2016**, *9* (4), 1412–1429 DOI: 10.1039/C6EE00129G.

(19) Park, Y.; McDonald, K. J.; Choi, K.-S. Progress in Bismuth Vanadate Photoanodes for Use in Solar Water Oxidation. *Chem. Soc. Rev.* **2013**, 2321–2337 DOI: 10.1039/c2cs35260e.

(20) Wenderich, K.; Mul, G. Methods, Mechanism, and Applications of Photodeposition in Photocatalysis: A Review. *Chem. Rev.* **2016**, acs.chemrev.6b00327 DOI: 10.1021/acs.chemrev.6b00327.

Chapter 2

Mechanistic details of the rate of hydrogen evolution from a suspension of rhodium-doped strontium titanate photocatalyst particles from photon flux dependencies on the internal quantum yield

Introduction

Sustainable methods for producing hydrogen are needed in order to reduce reliance on fossil fuels for energy and as a feedstock for the production of ammonia. Using a renewable energy source like solar or wind to drive electrolyzers that effect electrolysis of water, i.e. water splitting, are forecasted to be viable technoeconomic solutions capable of producing hydrogen on a cost equivalent basis to gallons of gasoline, but require advances in performance, durability, and cost.[1,2] Another option with a longer-term roadmap for cost effectiveness is the photocatalyst particle suspension reactor for solar water electrolysis.[3–6] This design consists of particles on the order of hundreds of nanometers to several microns that are wetted with water and each individually effect water electrolysis when illuminated, and this design represents a completely different form factor and engineering approach than photovoltaic-driven electrolysis and integrated photoelectrochemical designs. One design for a photocatalyst particle suspension reactor consists of two reactor compartments, one that contains particles that drive the hydrogen evolution reaction and another that contains particles that drive the oxygen evolution reaction. This tandem Z-scheme design separates the reactions to greatly help mitigate formation of explosive hazards consisting of mixture of H_2 and O_2, but it requires the added challenge of mediating electronic and ionic charge between the compartments via a soluble redox mediator.

Recent simulations of new designs for tandem Z-scheme reactors have suggested that the development of cost-effective hydrogen from these reactors may be easier than initially thought and that efficiency of the photocatalyst materials is the paramount challenge to attaining this goal.[7–9] Despite the apparent simplicity of Z-scheme particle suspension reactors, the solar-to-hydrogen conversion (STH) efficiency of such reactors has remained around 0.1% on the laboratory scale,[7] with a recent tandem demonstration consisting of both reactions occurring in one compartment using a photocatalyst sheet design that reported a 1% efficiency.[5,6] The need to enhance STH efficiency significantly motivates our work which is aimed at better understanding the mechanism of these state-of-the-art designs so that intentional and informed modifications can be made with the goal of increasing STH efficiency. Notably, most best-in-class demonstrations use doped $SrTiO_3$ to effect the hydrogen evolution reaction and $BiVO_4$ to effect the oxygen evolution reaction.[7] Details of the effectiveness of $BiVO_4$ have been studied extensively by the photoelectrochemistry community and therefore we decided to focus instead on details of doped $SrTiO_3$ for light-driven hydrogen evolution.[10–15]

The first demonstrations of photoelectrochemical (PEC) water electrolysis were conducted by Fujishima and Honda in the early 1970's using photoelectrodes.[16] While the first demonstrations of particle PEC water electrolysis were demonstrated in the late 1970's.[17–19] Each of the demonstrations using TiO_2 and relatively high energy photons, in the form of ultraviolet (UV) light, to produce hydrogen and oxygen. In more recent work, like that conducted by Ohtani and colleagues, much of the limitations associated with the use of TiO_2 in PEC water electrolysis were due to high concentrations of surface and bulk defects in the materials that acted as recombination centers for the photogenerated carriers.[20–22] Furthermore, work by Ohtani and others has led to a better understanding of the possible reaction mechanisms and rate laws

governing materials like TiO_2.[23,24] Metal oxides, like TiO_2, are candidate materials for PEC because they tend to be stable against (photo)corrosion. However, the strong bonding in these materials which contributes to their PEC stability and large bandgaps, leads to poor absorption outside of the UV region. To increase the rates of hydrogen production, doping with transition metals is often employed to expand the absorption range of materials into the visible spectrum and reduce the bandgap. Doped strontium titanates (X-doped $SrTiO_3$, where X is one or more transition metal dopants) are primary examples of these materials owing to their PEC stability, moderate bandgaps, and record rates of hydrogen production.[7] Kudo and colleagues are responsible for discovering and pioneering many of the state-of-the-art doped strontium titanates starting in the early 2010's.[25–29] Understanding the inherent limitations of these new materials, like their defect states which act as recombination centers, has led to the use of reducing atmospheres (hydrogen treatment) in materials like Rh-doped $SrTiO_3$ which has led to increased rates of hydrogen production.[25] Carrier doping, by using non-stoichiometric quantities of oxygen, has also been investigated leading to more than 40x the rate of hydrogen production as compared to materials with stoichiometric quantities of oxygen in $SrTiO_3$.[30] More recent work by Millet and others has revealed the influence of light intensity on these materials, as photoelectrodes. They show that despite increasing the concentration of photocarriers with increasing photon flux, the rate of hydrogen production decreases due to concomitant increase in carrier recombination due to high flux.[31] Therefore, investigation into the mechanisms and rate-laws of particulate Rh-doped $SrTiO_3$ loaded into aqueous media remains an area ripe for investigation.

The photoelectrochemistry community has amassed of suite of techniques to gain details on the causes of performance and mechanisms of action of photoelectrode materials.[32] However, all of these techniques require that one can monitor current and/or voltage of the illuminated

sample, which is a major feat for photocatalyst particles. Therefore, most studies of photocatalysts rely on monitoring the ultimate product of the reactions as a means to quantify effectiveness. By monitoring the rate of H_2 detected from a photocatalyst particle suspension as a function of one of several independent variables, information can be gleaned as to the processes by which the materials underwent light-driven reactivity.

To observe, this half-reaction, an electron donor is required as a complementary half reaction. This donor can either transfer charge reversibly or go through a series of reactions so that it is irreversible on the timescale of the rest of the photochemical processes. The irreversible sacrificial donor type systems enable one to study systems under lower light intensities where the small photon fluxes often limit net H_2 formation when active back reactions to the shuttle are operative. Herein, to better understand the underlying physical and chemical phenomena that limit the effectiveness of Rh-doped $SrTiO_3$ photocatalyst particles we used light-intensity-dependent studies of the yield for H_2 evolution, also as a function of the mass loading of the photocatalyst particles, and in the presence of sacrificial donor species.

Materials and Methods

Synthesis of Rh-doped $SrTiO_3$. The procedure for solid-state reaction (SSR) synthesis of rhodium-doped strontium titanate followed literature procedures.[33] Briefly, 0.790 g titanium dioxide, 1.583 g strontium carbonate, and 12.9 mg rhodium(III) oxide (1 mol % with respect to the amount of Ti atoms) are combined in a mortar. The mixture is ground manually for two hr until no brown streaks of rhodium oxide are visible in the off-white powder. The mixture is then sintered at 900 °C for 2 hr, followed by grinding again in a mortar for 15 min and subsequent sintering at 1100 °C for 10 hr.

Photochemical Pt deposition on Rh-doped $SrTiO_3$. 0.3 g of $SrTiO_3$:Rh(1 at%) material, 111 mL of 10% methanol in water, and 0.3 wt% platinum from an aqueous solution of hexachloroplatinic acid are combined in an optically transparent-sealable glass vessel. The solution is then continuously stirred and illuminated for 4 hr, using 1 sun illumination from a 150 W Xenon Arc Lamp with an AM1.5G filter (Oriel Instruments, Irvine, CA). Solid particles are collected via centrifugation, washed with water and then with ethanol to remove excess Pt reagent, and allowed to dry under ambient.

Calibration of the custom configured in-line mass spectrometer. The mass spectrometer (Hiden Analytic, Warrington, United Kingdom) was placed in-line to a quartz cuvette cell (FireFlySci, Staten Island, NY) used as the reaction vessel. The cell was maintained at approximately 1 atm of pressure with a continuous flow of 1.50 scfm of high purity argon gas. The rate of argon flow was carefully monitored as the apparatus was sensitive to changes in flow rate (**Figure S2.1**). In order to calculate accurate values for the rates of hydrogen production and associated quantum yields, the custom configured mass spectrometer and the photoelectrochemical cell used must be calibrated (**Figure 2.1**). To calibrate the system, a known quantity (in moles) of H_2 gas at ambient temperature and pressure is injected into the cell. An

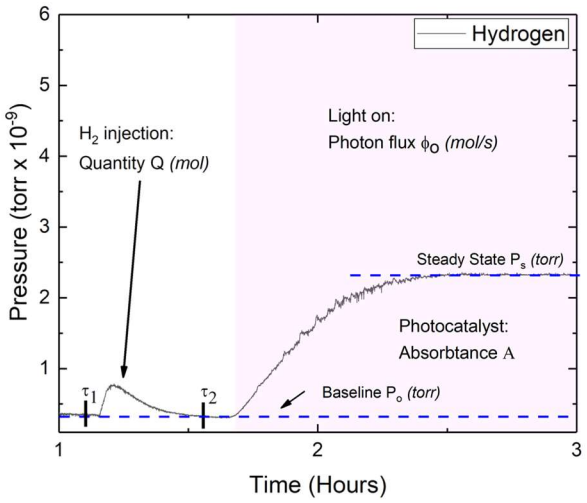

Figure 2.1. Calibration of photoelectrochemical cell with custom configured in-line mass spectrometer. The black line represents the hydrogen signal. The cell contains 2.0 mg of Rh-doped $SrTiO_3$ particles in 1 mL of 10% methanol solution. The light purple region represents the illuminated (light-on) response of the system to a 405 nm light source. The cell was injected with 5 µL of pure hydrogen at standard temperature and pressure.

instantaneous hydrogen injection rate can be determined by integrating the known moles, Q, injected into the cell between times τ_1 to τ_2 as given by

$$\text{Injection rate } \left(\frac{\text{mols}}{\text{sec}}\right) = R_i = \frac{Q}{\int_{\tau_1}^{\tau_2} dt} \tag{2.1}$$

where, R_i, is the instantaneous injection rate of hydrogen; Q, are the moles of pure hydrogen injected into the cell; and the integral in the denominator is the total time over which the injected hydrogen signal is observed between time points τ_1 to τ_2. Similarly, the average pressure for the instantaneous injection can be determined by

$$\text{Average calibration pressure (torr)} = P_{cal} = \frac{\int_{\tau_1}^{\tau_2} (P - P_0) dt}{\int_{\tau_1}^{\tau_2} dt} \tag{2.2}$$

where, P_{cal}, is the average instantaneous calibration pressure given in torr; the numerator represents the cumulative pressure over a given time interval with, P, the pressure at any particular instant less the baseline pressure, P_0; and the denominator is the total time over which the injected hydrogen signal is observed between time points τ_1 to τ_2. Using **Equations 2.1** and **2.2** the instrument sensitivity to hydrogen is given by

$$\text{Sensitivity } \left(\frac{\text{torr} * \text{sec}}{\text{mols}}\right) = S = \frac{P_{cal}}{R_i} \tag{2.3}$$

where, S, is the sensitivity of the given instrument and cell set-up for detection of hydrogen. Thus, once the sensitivity is determined the hydrogen generation rate is easily determined by

$$\text{Hydrogen generation rate } \left(\frac{\text{mols}}{\text{sec}}\right) = R_H = \frac{P_s - P_0}{S} \tag{2.4}$$

Where, R_H, is the hydrogen generation rate; P_S, is the steady state partial pressure for hydrogen in a given experiment; P_0, is again the baseline partial pressure of hydrogen. The custom measurement apparatus used for hydrogen detection was found to be in good agreement, 3.5% ±

0.3% EQY, with measurements for similar state-of-the-art materials found using gas chromatography and Schlenk lines, 3.9% - 4.2% EQY.[7]

Photochemical H_2 evolution analysis. Dried $SrTiO_3$:Rh(1 at%) particles (0.05 mg to 5.0 mg) are loaded into 1 mL of aqueous 10% methanol solution inside of the reaction vessel with a stir bar. The cell is maintained at approximately 1 atm of pressure with a continuous flow of argon gas. A 405 nm 1 W LED (Thorlabs) or a generic 405 nm 5 mW LED is used as a light source. To change light intensity or fluence an automated filter wheel was constructed to cycle through various neutral density (ND) filters (0.1 ND to 2 ND) (Thorlabs Inc., Newton, New Jersey) to attenuate the light source. Data was analyzed by calculating the internal quantum yield (IQY) for H_2 evolution as follows,

$$\mathrm{IQY} = \frac{2 \cdot R_{\mathrm{HER}}}{\Phi_{\mathrm{q}} \cdot \alpha} \tag{2.5}$$

where R_{HER} is the rate of hydrogen production (mol H_2/s), Φ_q is the photon flux (mol photon/s), and α is the absorptance of the semiconductor photocatalyst material as a fraction between 0 and 1.

Optical characterization. Particle loaded mixtures in cuvettes were characterized in custom 3D printed white polylactic acid (PLA) cuvette holders. Holders were generously coated with 6080 Diffuse White Reflective Coating (Labsphere, North Sutton, NH). Once coated, cuvette holders are assumed to approximate an integrating sphere as they are >99% reflective at 405 nm. Reflectance spectra for various mass loadings of particles in solution were sampled on a Jasco V-670 spectrophotometer with integrating sphere (Jasco Inc., Halifax, Nova Scotia, Canada) while under stirring at 1200 rpm using an inductive stir system (2MagUSA, Daytona Beach, FL).

Data Analysis. Data analysis was performed using custom scripts written in MATLAB (MathWorks, Natick, MA) and plotting data and curve fitting was performed using Origin Pro (OriginLab Corporation, Northampton, MA).

Results and Discussion

Synthesized $SrTiO_3$:Rh(1 at%) particles were characterized by x-ray diffraction (XRD) and scanning electron microscopy (SEM), and are consistent with previously reported literature (**Figure 2.2**).[33] The particles have a cuboid or globular shape and are polydispersed, consisting of individual and/or aggregates in the size range of 50 nm to tens of micrometers. The XRD reveals the perovskite crystal structure of the material with no traces of precursor impurities.

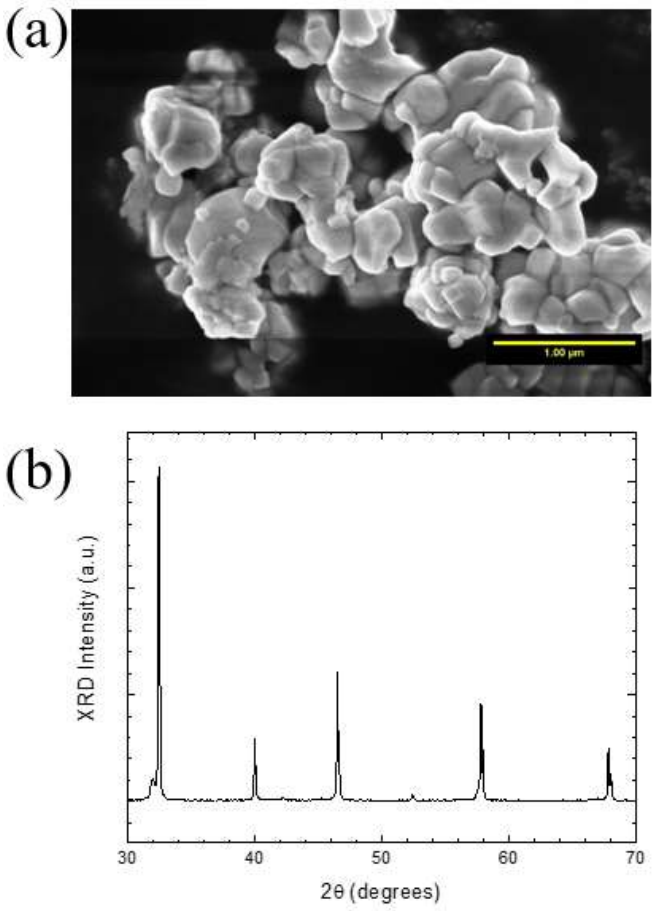

Figure 2.2. (a) Scanning electron micrograph and (b) X-ray diffraction spectrum of synthesized $SrTiO_3$:Rh(1 at%).

Solutions of varying $SrTiO_3$:Rh(1 at%) particle mass loading in 10% v/v methanol (aqueous) were characterized for their reflectance properties as illustrated in (**Figure S2.2**). The relationship between (particle) loading and reflectance is not linear across all ranges of concentration. When mass loading of particles is

relatively high (> 2 mg/mL) the assumption of absorptance equal to unity is approximately valid. However, the same assumption cannot be made for relatively low mass loadings of particles (< 2 mg/mL). This results in the external quantum yield being a poor figure of merit for dilute solutions and has implications for the

quantum yield as is discussed in detail later.

Photochemical tests of varying concentrations of *Pt (0.3 wt%)/SrTiO₃:Rh(1 at%)* all maintained the same general form for the hydrogen partial pressure (**Figure S2.3**). The results of varying the mass-loading of particles and varying the photon flux on the rate of hydrogen production, and external and internal quantum yields are found in (**Figure 2.3**). Sets of replicant

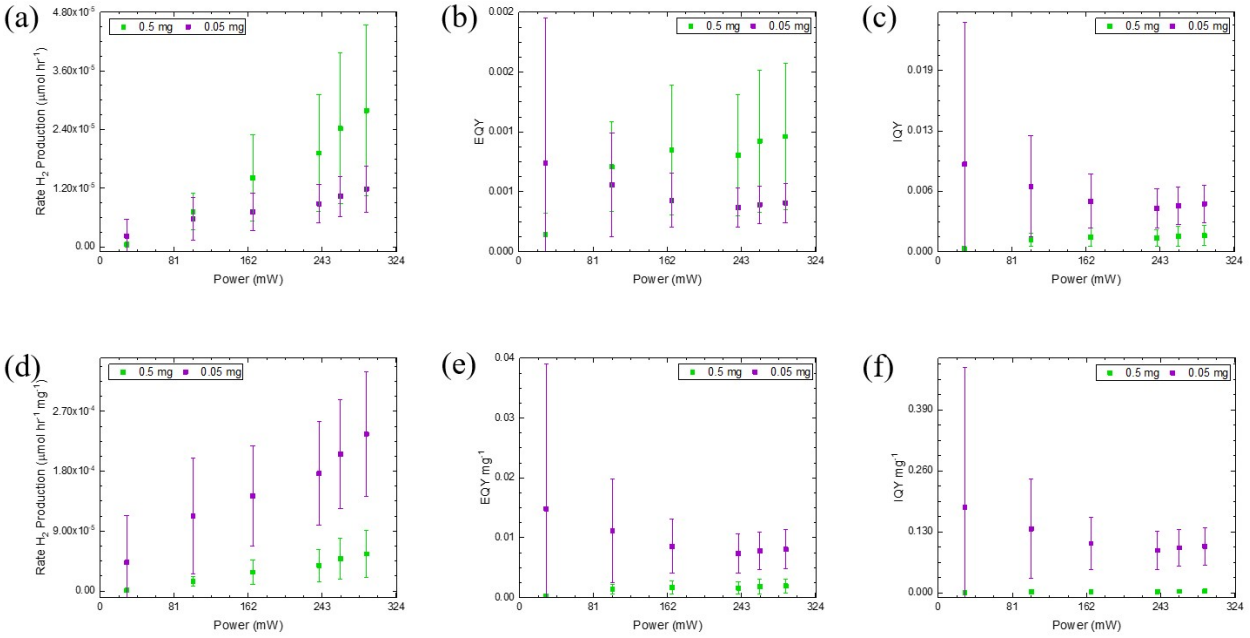

Figure 2.3. The (a) rate of hydrogen production, (b) the external quantum yield (EQY), (c) internal quantum yield (IQY), (d) rate of hydrogen production per mg, (e) EQY per mg ,and (f) IQY per mg as light power/flux is changed for 0.5 mg/mL and 0.05 mg/mL mass-loadings of Pt(0.3wt%)/$SrTiO_3$:Rh(1%) in 10% methanol (aqueous). Samples were continuously stirred and sparged with argon. A 405 nm (1 W LED) was used for illumination.

trials for high mass loading 0.5 mg (green markers) and for low mass loading 0.05 mg (purple markers) are shown. (**Figure 2.3** (a)) demonstrates that with increasing mass loading and increasing photon flux the rate of hydrogen production increases over the ranges tested. This is

consistent as an extensive property of the system, the more photocatalysts in the system for a given photon flux the more hydrogen that can be produced. Similarly, (**Figure 2.3** (b)) shows the same trends but for the EQY (where absorptance is assumed to be unity). However, in (**Figure 2.3** (c)) the IQY is different. The IQY functions more like an intrinsic figure of merit, it is a measure of the individual particle contribution to the quantum yield for a particular mass loading. In the case of low mass loading the individual contributions per particle are much higher than for high mass loadings due to decreased scattering (and low absorptance) (**Figure S2.2**). This result also suggests that at high mass loadings some of the particles in solution further away from the incident illumination may experience faster back reactions due to reduce flux from scattering. (**Figure 2.3** (d-f)) represents the data from (**Figure 2.3** (a-c)) but in terms of the individual mass loading contribution to the rate of hydrogen production, EQY, and IQY; respectively. On a per milligram (mg) basis, the rate of hydrogen production, EQY, and IQY are highest for low mass loadings at all light intensities. This suggests that both scattering and relatively fast reverse reactions (hydrogen oxidation) limit hydrogen production rates and quantum yields for high mass loading scenarios.

To further interrogate the activity of the Rh-doped $SrTiO_3$ at high/low mass loading and high/low flux, the log-log of each graph in (**Figure 2.3**) can be plotted as in (**Figure 2.4**). The log-log graphs may be interpreted the same as those in (**Figure 2.3**) because they are the same data represented different ways, i.e. linear vs log. However, the log-log data of the rate of hydrogen production vs photon flux power contains additional information— on the ratio of the orders of reaction contributing to catalysis and recombination relating to the general rate law for the hydrogen evolution reaction as discussed in detail in the **Supplementary Information**. Briefly, the rate of hydrogen production, which can be influenced by the absorptance properties

of the photocatalyst-solution mixture, is dictated by the kinetics and thus the mechanism of the hydrogen evolution reaction (HER). Generically, the HER rate may be given by

$$Rate_{HER} = k_{rec}[e^-]_{rec}^{v_{rec}} + k_{cat}[e^-]_{cat}^{v_{cat}} \quad (2.6)$$

where, k_{rec}, is the rate constant for recombination of electrons; $[e^-]_{rec}$ is the concentration of electrons that recombine with holes; ν_{rec}, is the order of $[e^-]_{rec}$; k_{cat}, is the rate constant for electrons at the surface; $[e^-]_{cat}$ is the concentration of electrons at the surface that go on to produce hydrogen through catalysis; ν_{cat}, is the order of $[e^-]_{cat}$. The rate of hydrogen production is the result of the rates of loss mechanisms. In the simplest generic case, **Equation 2.6**, the rate of production is assumed to consist only of losses due to recombination of charge carriers (first term) or due to production of hydrogen from successful catalysis (second term). Understanding the mechanism of the HER and its kinetics on photocatalysts can be exploited to maximize the rate of hydrogen production. In (**Figure 2.5**) the data appears to form two distinct regions based on differences in slope, region I at low (log(Power) < 2.24) and region II at high (log(Power) > 2.24) (**Table 2.1**). The smaller slope value in region I suggests that the order of electrons that recombine is greater than that of electrons used to catalyze hydrogen production. Region II suggests that the order of electrons used to catalyze hydrogen production is higher than the order for those electrons that recombine. Therefore, to maximize hydrogen production operation in region II is preferred. Further experiments are needed to yield more information about the non-generic rate law and to ascertain a reasonable mechanistic explanation for this behavior.

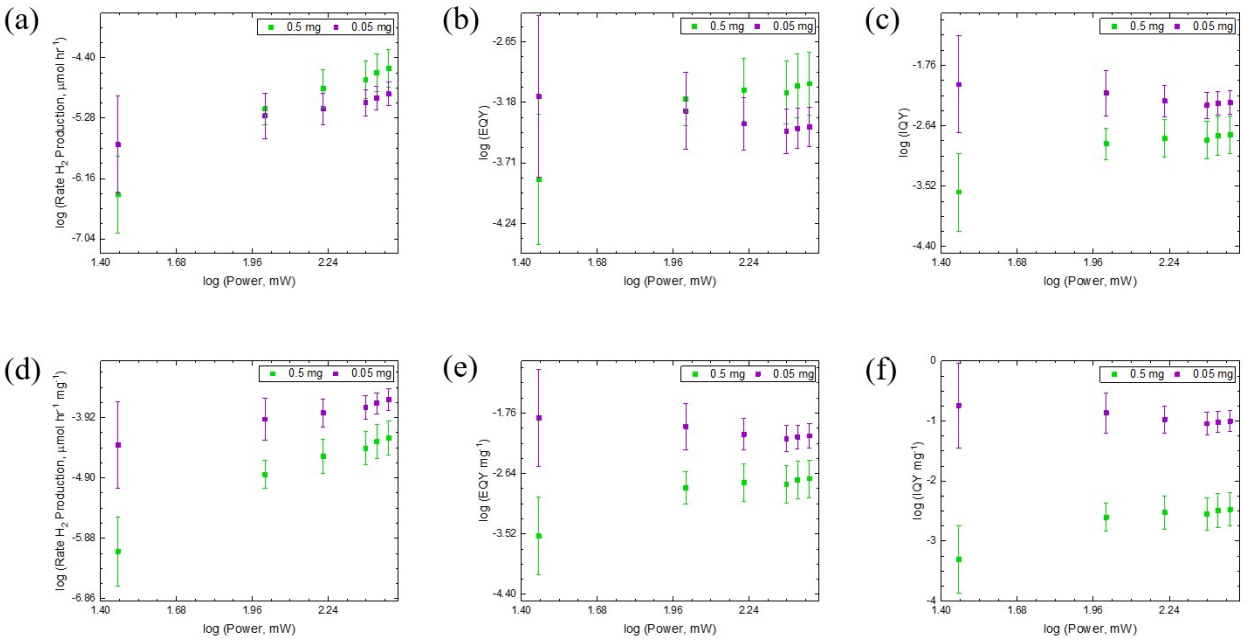

Figure 2.4. The log-log plots of (a) rate of hydrogen production, (b) the external quantum yield (EQY), (c) internal quantum yield (IQY), (d) rate of hydrogen production per mg, (e) EQY per mg ,and (f) IQY per mg as light power/flux is changed for 0.5 mg/mL and 0.05 mg/mL mass-loadings of Pt(0.3wt%)/$SrTiO_3$:Rh(1%) in 10% methanol (aqueous). Samples were continuously stirred and sparged with argon. A 405 nm (1 W LED) was used for illumination.

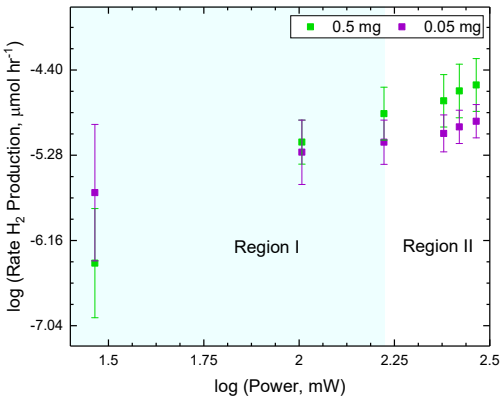

Figure 2.5. The log-log plot of the rate of hydrogen production as light power/flux is changed for 0.5 mg/mL and 0.05 mg/mL mass-loadings of Pt(0.3wt%)/$SrTiO_3$:Rh(1%) in 10% methanol (aqueous). Samples were continuously stirred and sparged with argon. A 405 nm (1 W LED) was used for illumination. (Light blue shading) Region I. (White background) Region II.

Table 2.1. The average values of slope and intercept for regions I & II in (**Figure 2.5**).

Mass Loading (mg/mL)	Region I		Region II	
	Slope	Intercept	Slope	Intercept
0.5	2.0 ± 0.4	-9.2 ± 0.7	1.9 ± 0.3	-9.3 ± 0.8
0.05	0.7 ± 0.1	-6.6 ± 0.2	1.5 ± 0.1	-8.5 ± 0.2

Conclusion

In this work we have shown that it is possible to glean some reaction order related information for the hydrogen evolution reaction from particles loaded in solution using in-line mass spectrometry. It appears that there are at least two photon flux regions high/low in the ranges tested, in which the ratio for the orders of reaction for catalysis and recombination change. This change in reaction order coupled with information from scattering and quantum yields can be used to optimize the rate of hydrogen production within various photon flux and mass loading regimes.

Acknowledgements

The author would like to thank Zejie Chen for assistance with some of the later photochemical experiments in this work. A big thank you to Professor Akihiko Kudo's group for both providing samples and training to W.G. on the synthesis of Rh-doped $SrTiO_3$. Dr. Dmitry Fishman for generous use of the Laser Spectroscopy Lab at UC Irvine's instruments.

References

(1) Energy, D. of. *Hydrogen Production Technical Team Roadmap June 2013*; 2013.

(2) Ardo, S.; Rivas, D. F.; Modestino, M. A.; Schulze, V.; Mei, B.; Miller, E. L.; Moore, G. F.; Muller, J.; Orchard, K. L.; Rosser, T. E.; et al. Pathways to Electrochemical Solar-Hydrogen Technologies. *Energy Environ. Sci.* **2018**, *11* (10), 2768–2783. https://doi.org/10.1039/c7ee03639f.

(3) James, B. D.; Baum, G. N.; Perez, J.; Baum, K. N. Technoeconomic Analysis of Photoelectrochemical (PEC) Hydrogen Production. *DOE Contract Number GS-10F-009J* **2009**, *22201* (December), 1–128.

(4) Pinaud, B. A.; Benck, J. D.; Seitz, L. C.; Forman, A. J.; Chen, Z.; Deutsch, T. G.; James, B. D.; Baum, K. N.; Baum, G. N.; Ardo, S.; et al. Technical and Economic Feasibility of Centralized Facilities for Solar Hydrogen Production via Photocatalysis and Photoelectrochemistry. *Energy Environ. Sci.* **2013**, *6* (7), 1983. https://doi.org/10.1039/c3ee40831k.

(5) Wang, Q.; Hisatomi, T.; Jia, Q.; Tokudome, H.; Zhong, M.; Wang, C.; Pan,

Z.; Takata, T.; Nakabayashi, M.; Shibata, N.; et al. Scalable Water Splitting on Particulate Photocatalyst Sheets with a Solar-to-Hydrogen Energy Conversion Efficiency Exceeding 1%. *Nat. Mater.* **2016**, *15* (March), 1–3. https://doi.org/10.1038/nmat4589.

(6) Goto, Y.; Hisatomi, T.; Wang, Q.; Higashi, T.; Ishikiriyama, K.; Maeda, T.; Sakata, Y.; Tokudome, H.; Katayama, M.; Akiyama, S.; et al. A Particulate Photocatalyst Water-Splitting Panel for Large-Scale Solar Hydrogen Generation. *Joule* **2018**, *2* (3), 509–520. https://doi.org/10.1016/j.joule.2017.12.009.

(7) Fabian, D. M.; Hu, S.; Singh, N.; Houle, F. A.; Hisatomi, T.; Domen, K.; Osterloh, F. E.; Ardo, S. Particle Suspension Reactors and Materials for Solar-Driven Water Splitting. *Energy Environ. Sci.* **2015**, *8*, 2825–2850. https://doi.org/10.1039/c5ee01434d.

(8) Chandran, R. B.; Breen, S.; Shao, Y.; Ardo, S.; Weber, A. Z. Evaluating Particle-Suspension Reactor Designs for Z-Scheme Solar Water Splitting via Transport and Kinetic Modeling. *Energy Environ. Sci.* **2018**, *11* (1), 115–135. https://doi.org/10.1039/c7ee01360d.

(9) Keene, S.; Chandran, R. B.; Ardo, S. Calculations of Theoretical Efficiencies for Electrochemically-Mediated Tandem Solar Water Splitting as a Function of Bandgap Energies and Redox Shuttle Potential. *Energy Environ. Sci.* **2019**, *12*, 261–272. https://doi.org/10.1039/c8ee01828f.

(10) Newhouse, P. F.; Guevarra, D.; Umehara, M.; Boyd, D. A.; Zhou, L.; Cooper, J. K.; Haber, J. A.; Gregoire, J. M. Multi-Modal Optimization of Bismuth Vanadate Photoanodes via Combinatorial Alloying and Hydrogen Processing. *Chem. Commun.* **2019**, *55* (4), 489–492. https://doi.org/10.1039/c8cc07156j.

(11) Toma, F. M.; Cooper, J. K.; Kunzelmann, V.; McDowell, M. T.; Yu, J.; Larson, D. M.; Borys, N. J.; Abelyan, C.; Beeman, J. W.; Yu, K. M.; et al. Mechanistic Insights into Chemical and Photochemical Transformations of Bismuth Vanadate Photoanodes. *Nat. Commun.* **2016**, *7* (May). https://doi.org/10.1038/ncomms12012.

(12) Nair, V.; Perkins, C. L.; Lin, Q.; Law, M. Textured Nanoporous Mo:BiVO4 Photoanodes with High Charge Transport and Charge Transfer Quantum Efficiencies for Oxygen Evolution. *Energy Environ. Sci.* **2016**, *9* (4), 1412–1429. https://doi.org/10.1039/c6ee00129g.

(13) Kim, T. W.; Ping, Y.; Galli, G. A.; Choi, K. S. Simultaneous Enhancements in Photon Absorption and Charge Transport of Bismuth Vanadate Photoanodes for Solar Water Splitting. *Nat. Commun.* **2015**, *6*, 1–10. https://doi.org/10.1038/ncomms9769.

(14) Park, Y.; McDonald, K. J.; Choi, K. S. Progress in Bismuth Vanadate Photoanodes for Use in Solar Water Oxidation. *Chem. Soc. Rev.* **2013**, *42* (6), 2321–2337. https://doi.org/10.1039/c2cs35260e.

(15) Park, Y.; Kang, D.; Choi, K. S. Marked Enhancement in Electron-Hole Separation Achieved in the Low Bias Region Using Electrochemically Prepared Mo-Doped BiVO4 Photoanodes. *Phys. Chem. Chem. Phys.* **2014**, *16* (3), 1238–1246. https://doi.org/10.1039/c3cp53649a.

(16) Fujishima, A.; Honda, K. Electrochemical Photolysis of Water at a Semiconductor Electrode. *Nature* **1972**, *238*, 37–38.

(17) Kawai, T.; Sakata, T. Photocatalytic Decomposition of Gaseous Water over TiO2 and TiO2-RuO2 Surfaces. *Chem. Phys. Lett.* **1980**, *72* (1), 87–89. https://doi.org/10.1016/0009-2614(80)80247-8.

(18) Van Damme, H.; Hall, W. K. On the Photoassisted Decomposition of Water at the Gas-Solid Interface on TiO2. *J. Am. Chem. Soc.* **1979**, *101* (15), 4373–4374. https://doi.org/10.1021/ja00509a055.

(19) Schrauzer, G. N.; Guth, T. D. Photolysis of Water and Photoreduction of Nitrogen on Titanium Dioxide1. *J. Am. Chem. Soc.* **1977**, *99* (22), 7189–7193. https://doi.org/10.1021/ja00464a015.

(20) Ohtani, B.; Ogawa, Y.; Nishimoto, S. I. Photocatalytic Activity of Amorphous-Anatase Mixture of Titanium(IV) Oxide Particles Suspended in Aqueous Solutions. *J. Phys. Chem. B* **1997**, *101* (19), 3746–3752. https://doi.org/10.1021/jp962702+.

(21) Kominami, H.; Murakami, S. Y.; Kato, J. I.; Kera, Y.; Ohtani, B. Correlation between Some Physical Properties of Titanium Dioxide Particles and Their Photocatalytic Activity for Some Probe Reactions in Aqueous Systems. *J. Phys. Chem. B* **2002**, *106* (40), 10501–10507. https://doi.org/10.1021/jp0147224.

(22) Prieto-Mahaney, O. O.; Murakami, N.; Abe, R.; Ohtani, B. Correlation between Photoeatalytic Activities and Structural and Physical Properties of

Titanium(IV) Oxide Powders. *Chem. Lett.* **2009**, *38* (3), 238–239. https://doi.org/10.1246/cl.2009.238.

(23) Zhang, M.; Frei, H. Water Oxidation Mechanisms of Metal Oxide Catalysts by Vibrational Spectroscopy of Transient Intermediates. *Annu. Rev. Phys. Chem.* **2017**, *68* (1), 209–231. https://doi.org/10.1146/annurev-physchem-052516-050655.

(24) Takeuchi, S.; Takashima, M.; Takase, M.; Ohtani, B. Digitally Controlled Kinetics of Titania-Photocatalyzed Oxygen Evolution. *Chem. Lett.* **2018**, *47*, 373–376. https://doi.org/10.1246/cl.171093.

(25) Niishiro, R.; Tanaka, S.; Kudo, A. Hydrothermal-Synthesized SrTiO3 Photocatalyst Codoped with Rhodium and Antimony with Visible-Light Response for Sacrificial H2 and O2 Evolution and Application to Overall Water Splitting. *Appl. Catal. B Environ.* **2014**, *150–151*, 187–196. https://doi.org/10.1016/j.apcatb.2013.12.015.

(26) Antuch, M.; Millet, P.; Iwase, A.; Kudo, A.; Grigoriev, S. A.; Voloshin, Y. Z. Characterization of Rh:SrTiO3 Photoelectrodes Surface-Modified with a Cobalt Clathrochelate and Their Application to the Hydrogen Evolution

Reaction. *Electrochim. Acta* **2017**, *258*, 255–265. https://doi.org/10.1016/j.electacta.2017.10.018.

(27) Suzuki, S.; Matsumoto, H.; Iwase, A.; Kudo, A. Enhanced H2 Evolution over an Ir-Doped SrTiO3 Photocatalyst by Loading of an Ir Cocatalyst Using Visible Light up to 800 Nm. *Chem. Commun.* **2018**, *54* (75), 10606–10609. https://doi.org/10.1039/c8cc05344h.

(28) Murthy, D. H. K.; Matsuzaki, H.; Wang, Q.; Suzuki, Y.; Seki, K.; Hisatomi, T.; Yamada, T.; Kudo, A.; Domen, K.; Furube, A. Revealing the Role of the Rh Valence State, La Doping Level and Ru Cocatalyst in Determining the H 2 Evolution Efficiency in Doped SrTiO 3 Photocatalysts. *Sustain. Energy Fuels* **2019**, *3* (1), 208–218. https://doi.org/10.1039/c8se00487k.

(29) Kudo, A.; Yoshino, S.; Tsuchiya, T.; Udagawa, Y.; Takahashi, Y.; Yamaguchi, M.; Ogasawara, I.; Matsumoto, H.; Iwase, A. Z-Scheme Photocatalyst Systems Employing Rh- and Ir-Doped Metal Oxide Materials for Water Splitting under Visible Light Irradiation. *Faraday Discuss.* **2019**, *215*, 313–328. https://doi.org/10.1039/c8fd00209f.

(30) Nishioka, S.; Hyodo, J.; Vequizo, J. J. M.; Yamashita, S.; Kumagai, H.;

Kimoto, K.; Yamakata, A.; Yamazaki, Y.; Maeda, K. Homogeneous Electron Doping into Non-Stoichiometric Strontium Titanate Improves Its Photocatalytic Activity for Hydrogen and Oxygen Evolution. *ACS Catal.* **2018**, *8*, 7190–7200. https://doi.org/10.1021/acscatal.8b01379.

(31) Antuch, M.; Kudo, A.; Millet, P. Influence of Light Intensity on the Kinetics of Light-Driven Hydrogen Evolution Using Rh-Doped SrTiO 3 : A Study by Photoelectrochemical Impedance Spectroscopy. **2017**, *49* (C), 95–101.

(32) Chen, Z.; Dinh, H. N.; Miller, E. *Photoelectrochemical Water Splitting: Standards, Experimental Methods, and Protocols*; Springer: New York, 2013. https://doi.org/10.1007/978-1-4614-8298-7.

(33) Konta, R.; Ishii, T.; Kato, H.; Kudo, A. Photocatalytic Activities of Noble Metal Ion Doped SrTiO3 under Visible Light Irradiation. *J. Phys. Chem. B* **2004**, *108* (26), 8992–8995. https://doi.org/10.1021/jp049556p.

Supplementary Information

Accounting for the flow rate in the calibration of the customized apparatus

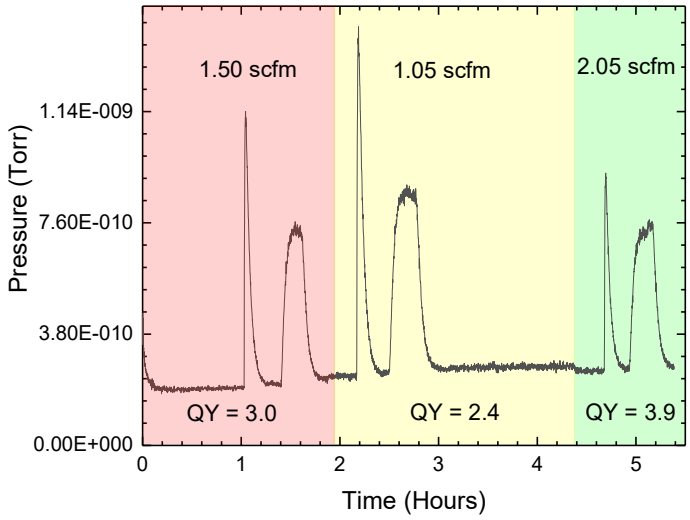

Figure S2.1. Effects on hydrogen signal and quantum yield by varying the argon carrier gas for a sample of 2 mg/mL loaded particles of Pt(0.3 wt%)/$SrTiO_3$:Rh(1 at%) in 10% v/v methanol (aqueous). Illuminated with a 405 nm light source and continuously stirred.

Following the procedures outlined for the general calibration (above), it is found that adjusting the flow rate of argon gas effects the apparent rate of hydrogen production and associated quantum yields (**Figure S2.1**). All measurements reported in this work utilized a flow rate of 1.50 scfm.

Reflectance (absorptance) of various mass loadings

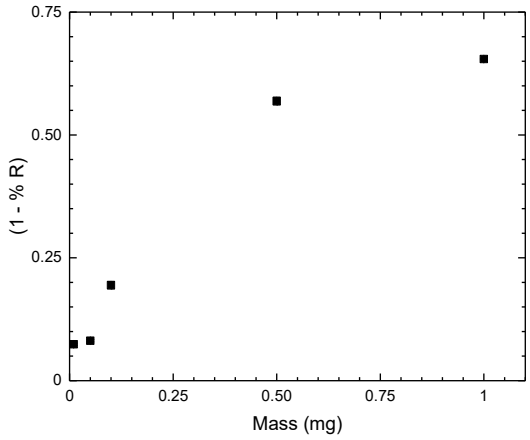

Figure S2.2. Reflectance values for various concentrations of Pt(0.3 wt%)/$SrTiO_3$:Rh (1 at%) in 10% v/v methanol (aqueous) at 405 nm and continuously stirred.

The absorptance values used in the internal quantum yield calculations assumed that the incident light was only subject to scattering or absorption. Thus, (1 -%R) was taken as the absorptance.

Photochemical Experiment Data

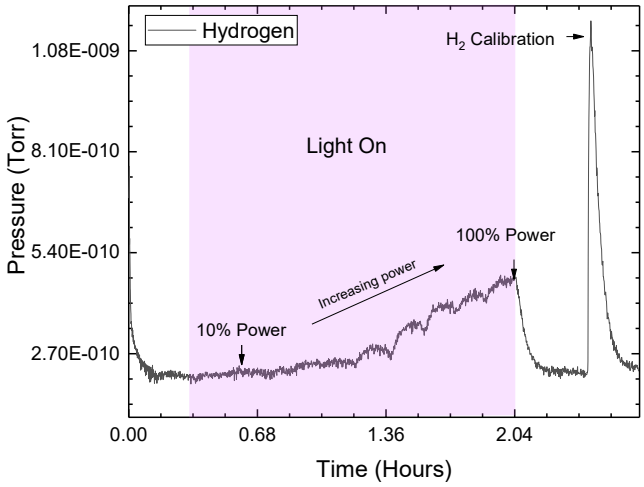

Figure S2.3. Light on-off experiment with change in photon flux. (Black line) Partial pressure of hydrogen in a continuously stirred 2 mg/mL Pt(0.3 wt%)/$SrTiO_3$:Rh (1 at%) in 10% v/v methanol (aqueous) solution. The light purple region represents the light-on behavior during illumination with a 405 nm LED light source. The second hydrogen peak on the right is a representative calibration.

The results of a general photochemical experiment run are seen. As the photon flux/power is sequentially stepped toward increasing photon flux/power (purple shaded region) the hydrogen signal rises and will plateau if given enough time at a given step.

Development of a generic rate law for HER

Assuming all photogenerated carriers either recombine or catalyze hydrogen evolution, the simplest generic rate law that can be developed and interrogated for the system under consideration in this experiment is

$$Photon\ Flux\ Generation = k_{rec}[e^-]_{rec}^{\nu_{rec}} + k_{cat}[e^-]_{cat}^{\nu_{cat}} \quad \text{(S2.1)}$$

where, Photon Flux Generation, is the rate of generated carriers due to a given flux impinging on the photocatalyst particles in solution; k_{rec}, is the rate constant for recombination of electrons; [e-]rec is the concentration of electrons that recombine with holes; ν_{rec}, is the order of [e-]rec; kcat, is the rate constant for electrons at the surface; $[e^-]_{cat}$ is the concentration of electrons at the surface that go on to produce hydrogen through catalysis; ν_{cat}, is the order of $[e^-]_{cat}$. The photon flux generation is the sum of the photogenerated carriers that recombine (first term) and the carriers that are consumed in catalyzing water to hydrogen (second term). As the EQY is less than 5%, an assumption can be made about the relative rates of catalysis and recombination such that

$$rate_{cat} \ll rate_{rec} \quad \text{(S2.2)}$$

Therefore, a simplification of **Equation S2.1** can be made where catalysis is assumed to be negligible, such that

$$Photon\ Flux\ Generation \approx k_{rec}[e^-]_{rec}^{\nu_{rec}} \quad \text{(S2.3)}$$

With minor rearrangement, the concentration of electrons can be thought of as a function of the photon flux generation, as in

$$[e^-] = \left(\frac{Photon\ Flux}{k_{rec}}\right)^{\left(\frac{1}{\nu_{rec}}\right)} \quad \text{(S2.4)}$$

As the mass spectrometer is only able to detect the products of catalysis, i.e. hydrogen, the hydrogen signal detected is proportional only to the portion of the rate law responsible for catalysis as given by

$$\text{Mass Spectrometer}_{\text{Hydrogen Partial Pressure}} \propto k_{cat}[e^-]_{cat}^{\nu_{cat}} \tag{S2.5}$$

An assumption can be made about the concentration of electrons involved in catalysis and those involved in recombination so that the mass spectrometer hydrogen signal is a function only of the photon flux and orders/constants related to catalysis and recombination, given by

$$\text{Assume: } [e^-]_{surf} = [e^-]_{rec} \tag{S2.6}$$

Then,

$$\text{Mass Spectrometer}_{\text{Hydrogen Partial Pressure}} \propto k_{cat}[\left(\frac{Photon\ Flux}{k_{rec}}\right)^{\left(\frac{1}{\nu_{rec}}\right)}]^{\nu_{cat}} \tag{S2.7}$$

Taking, the logarithm of both sides of the equation after rearrangement yields

$$\log(\text{Mass Spec}) = \frac{\nu_{cat}}{\nu_{rec}}\log(photon\ flux) + \log\left(k_{cat}\left(\frac{1}{k_{rec}}\right)^{\left(\frac{\nu_{cat}}{\nu_{rec}}\right)}\right. \tag{S2.8}$$

The result, **Equation S2.8**, is the equation of a line (Y = mx +b). Where, Y, is the log(Mass Spec); the slope of the line, m, is $\frac{\nu_{cat}}{\nu_{rec}}$, and b is $\log\left(k_{cat}\left(\frac{1}{k_{rec}}\right)^{\left(\frac{\nu_{cat}}{\nu_{rec}}\right)}\right.$. Thus, a log-log plot of the rate of hydrogen production versus the photon flux can provide some insight into the kinetics of the hydrogen evolution reaction.

Chapter 3

Modulating the density of states in mesoporous thin films of nanocrystalline TiO2 with Lewis acidic cations and hydroxide anions

Introduction

Increased implementation of renewable sources of energy such as wind and solar are helping to curb greenhouse gas emissions and their impact on the environment. While renewables are both freely available and carbon neutral, their widespread implementation still presents significant challenges, such as difficulties in implementing intermittent power into the grid and their lack of inherent storage options to time-shift energy supply to better match demand. Pumped hydro and solid-state batteries are two possible energy storage solutions, but they have significant geographical, scalability, and cost hurdles. Redox flow battery (RFB) and redox flow capacitor (RFC) technologies are possibly technoeconomically feasible mid-to-large-scale energy storage solutions for intermittent renewable energy sources. Unlike solid-state batteries, RFBs and RFCs consist of an electrochemical cell where the storage media is transferred into and out of the cell, meaning that energy and power are decoupled so that systems can be easily scaled to meet specific needs. Energy density in these systems is dictated by the volume of redox active species in the posolyte and negolyte, which are physically separated and pumped into an electrochemical cell where the redox active species undergo redox reactions to charge or discharge. The power output in these systems is a function of the electroactive area of the electrodes and the rate of flow of redox active species, which allows for variability in power output and decoupling it from the energy storage of the system.[1]

While pure RFBs and RFCs perform redox reactions with solution-phase species, many redox couples that are amenable to RFBs and RFCs require that at least one redox reaction involve a solid reactant or product. When this is the case, these so-called hybrid RFBs and RFCs lose the advantage of fully decoupling the energy density and power density. One way to overcome this limitation is to utilize semi-solid flowable versions of solid-state redox-active materials. In this way, the solid species can still be stored external to the electrochemical cell and the advantages of decoupling energy density and power density still exist. While this concept is somewhat nascent, recent demonstrations show promise for such a concept.[2]

Mid-to-large-scale energy storage will require large volumes of electrolyte and for this reason, the only option that makes economic sense is to use water. While water is ubiquitous and benign, it suffers from having a rather small electrochemical stability window, meaning that the potential difference required to oxidize and reduce water is rather small, E_{cell} = 1.23 V. While this can in part be overcome through use of electrode materials that are kinetically sluggish at performing these redox reactions, the voltage is still limited to <2 V where in comparison, Li ion batteries, which are based on non-aqueous electrolytes, can exceed two times this value. This critical gap limits the energy density of aqueous RFBs and RFCs. Moreover, materials for use in semi-solid flowable RFBs and RFCs are chosen based on the location of their band-edge positions relative to the potentials for performing redox with H_2 and O_2. This aids in the identification of promising materials and rules out the use of others. While often a fair first-order approximation many times the observed redox potentials of certain materials is highly influenced by the nature of the Lewis acidic cations present in the aqueous solutions. For example, in dye-sensitized solar cells using nitrile-based solvents, small Lewis acidic cations can modulate the potential of the density of states in the underlying semiconducting TiO_2 substrate.[3] In aqueous

solutions, protons are able to serve in a similar role. However, less is known about the interplay of Lewis acidic cations and protons present simultaneously in aqueous electrolytes.

These facts motivated my work into assessing the potential-determining effects of ions in water also in the presence of small Lewis acidic cations. Notably, we hypothesized that by use of alkaline electrolytes, the effect of proton activity on the energetics of the states in TiO_2 could be lessened so that the effect of Lewis acidic cations in water could be observed. Using electronic absorption spectroscopy in combination with potential-step chronoamperometry, i.e. spectroelectrochemistry, the density of states of electrons near the conduction band edge of TiO_2 were probed as the potential was negatively polarized.

Materials and Methods

Titanium dioxide paste. The TiO_2 paste used here followed literature procedures outlined in Ito, et al. with the substitution of commercially available Aeroxide p25 (anatase phase) TiO_2 (ACROS Organics, Waltham, MA) instead of synthesizing TiO_2 from scratch.[4]

Electrode Preparation. Electrodes were prepared by doctor blading TiO_2 paste onto TEC-15 fluorine-doped tin oxide (FTO) (Hartford Glass, Hartford City, Indiana) that had been masked using Scotch brand tape. After a brief drying period in air, a muffle furnace (Paragon, Mesquite, TX) was used to anneal the electrodes. The electrodes were ramped from room temperature at a rate of 500 °C/hr to 90 °C and held at temperature for 20 min. Subsequently, the electrodes were ramped at a rate of 500 °C/hr to 500 °C and held at temperature for 1 hr; then allowed to cool naturally to room temperature. Upon cooling to room temperature, all electroactive portions of the electrode other than the TiO_2 that would be exposed to an aqueous environment were epoxied

using Loctite Hysol 1C-LV (Henkel Co., Westlake, OH). The epoxy was then cured per manufacturer specifications prior to electrode use..

Solution Preparation. Aqueous sodium hydroxide solutions at approximate pH values of 8, 10, 12, and 13 were prepared by adding the appropriate amount of anhydrous sodium hydroxide to MilliQ filtered water until the pH reading held a persistent value on a pH meter (Oakton, Vernon Hills, IL). 100 mM Na^+, as sodium perchlorate, was added to solutions of pH values 8, 10, and 12 in order to approximate the cation concentration and ionic strength of pH 13 solution.

Spectroelectrochemical Setup. The TiO_2 on FTO (hereafter referred to as TiO_2/FTO) was used as the working electrode, a platinum mesh as the counter electrode, and a saturated KCl calomel electrode (SCE) as a reference electrode (CH Instruments Inc., Austin, TX). Prior to experimentation the spectroelectrochemical cell containing electrodes and solution were sparged for 10 min with argon and continuously thereafter throughout the experiments. A Cary 60 UV-Vis spectrophotometer (Agilent Technologies, Santa Clara, CA) was used in tandem with a VSP-300 potentiostat (Bio-Logic Science Instruments, Seyssinet-Pariset, France) to gather spectroelectrochemical data. The spectrophotometer was set to continuously scan, on "fast mode," the absorbance throughout the experiment from 1100 – 200 nm at 0.2 min per scan. Prior to measurements the instrument was baselined on air. The protocol on the potentiostat was automated to sequentially perform cathodic chronoamperometry experiments from 0 V to -1.9 V *vs* SCE in steps of 50 – 100 mV.

Data Analysis. All results contained herein utilized custom MATLAB (MathWorks, Natick, MA) scripts for data analysis and Origin Pro (OriginLab Corporation, Northampton, MA) for graphing and curve fitting.

Results and Discussion

As the potential of the TiO_2/FTO electrode is stepped more negative the occupancy of states near the conduction band (CB) edge increases resulting in an increase in the absorbance of the sample due to absorption transitions to states of higher energy in the CB. A wavelength often used to quantify the concentration of electrons in these states is 800 nm, although most wavelengths exhibit new absorption transitions due to electronic occupancy of these states. Typically, these measurements are conducted in polar aprotic electrolyte solutions and the relationship between this absorbance and the applied potential bias takes the form of an exponential with a non-ideal thermodynamic stretch parameter that has been previously ascribed to a density of trap states that lies several hundred millivolts below the conduction band edge of TiO_2. Herein we conducted measurements using aqueous electrolytes and instead observed a sigmoidal relationship between this absorbance and the applied potential bias. Applied potentials more positive than -1.0 V vs SCE resulted in little-to-no change in absorbance and the characteristic exponential-shaped data was observed between -1.0 V and -1.8 V *vs* SCE. However, at applied potentials more negative than -1.8V *vs* SCE the absorbance remained nearly unchanged. This observation is consistent with a rapid rate of electron transfer to evolve H_2 using these electrons populated near the conduction band such that even when the Fermi level at the FTO contact is increased, a substantial increase in the concentration of electrons in states near the conduction band edge could not be populated. Evidence for enhanced H_2 evolution was apparent from visual observation of

bubble formation at the TiO_2 surface.

Using the difference in absorbance at 800 nm as a function of applied potential bias, the cumulative effective density of states can easily be calculated as a function of the applied potential bias, as described in the supplementary section and previously. A series of cumulative effective density of states plots were determined for several pH values ranging from 8 to 13. These data showed two general effects based on the pH regime. At less basic pH values of 8 – 10, the density of states were nearly independent of the pH of the aqueous supporting electrolyte, behavior that is consistent with an aprotic species dictating their energetic location. Because Lewis acidic cations are known to influence the density of states we assume that the Lewis acidic Na^+ dictates the potential required to reduce the vacant states in TiO_2 near the conduction band edge. This is logical because at these pH values the concentration of H+ is ~<10^{-8} M while the concentration of Na^+ is 10^{-1} M. Interestingly, at more basic pH values of 12 – 13, the density of states depended on the pH of the aqueous supporting electrolyte, behavior that is consistent with a protic species dictating their energetic location. While cations are typically thought to be

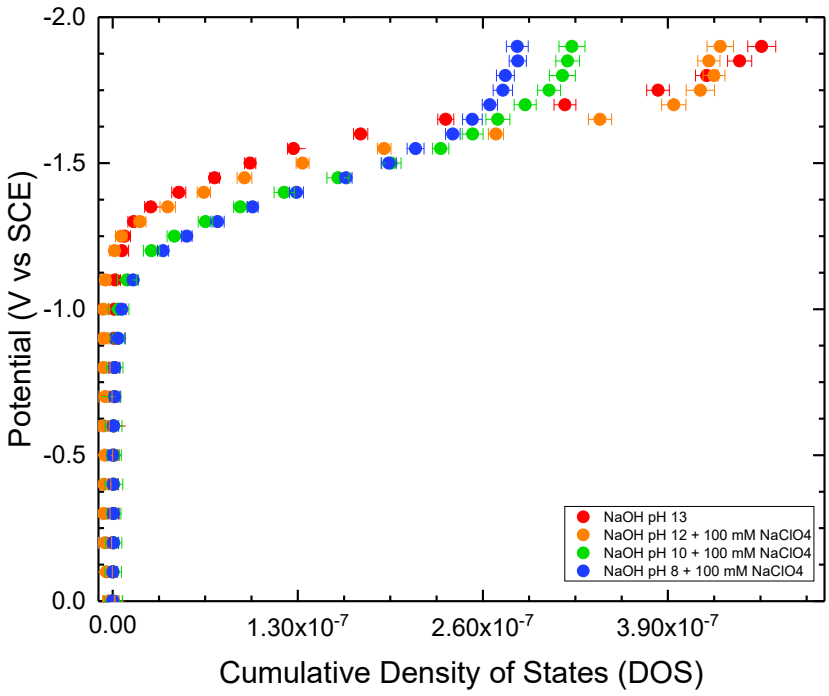

Figure 3.1. Cumulative thermodynamically accessible density of states near the conduction band edge of nanocrystalline TiO_2 cast as mesoporous thin films and immersed in aqueous sodium hydroxide solutions at the indicated pH values. Potential values are versus the saturated calomel electrode (SCE).

responsible for modulations in the density of states near the conduction band edge, in this case the concentration of H^+ is $\sim<10^{-11}$ M while the concentration of Na^+ remained at 10^{-1} M. The most logical explanation for this observation is that aqueous OH^-, and not H+, dictate the density of states near the conduction band edge. Their concentration ranges from 10^{-3} to 10^{-1} M, which is much closer to the concentration of Na^+. At low bias (0V vs SCE to -1V vs SCE) and despite changes to pH, the DOS between samples appears to remain largely the same. However, upon increasing the negative bias on TiO_2 in pH 13 and pH 12 NaOH solutions are potentially determined by hydroxide ions in solution. In this regime of bias, the pH 10 and pH 8 solutions require less bias (< 150 mV) to achieve the same DOS as the more alkaline solutions tested. At much greater bias, the pH 13 and pH 12 NaOH solutions are capable of sustaining a greater density of states than the more acidic solutions, in part because little to no hydrogen evolution occurs in such alkaline conditions. However, since hydrogen evolution is sensitive to pH changes and consequently occurs at different potentials, a more informative understanding can be gleaned from a graph of the density of states

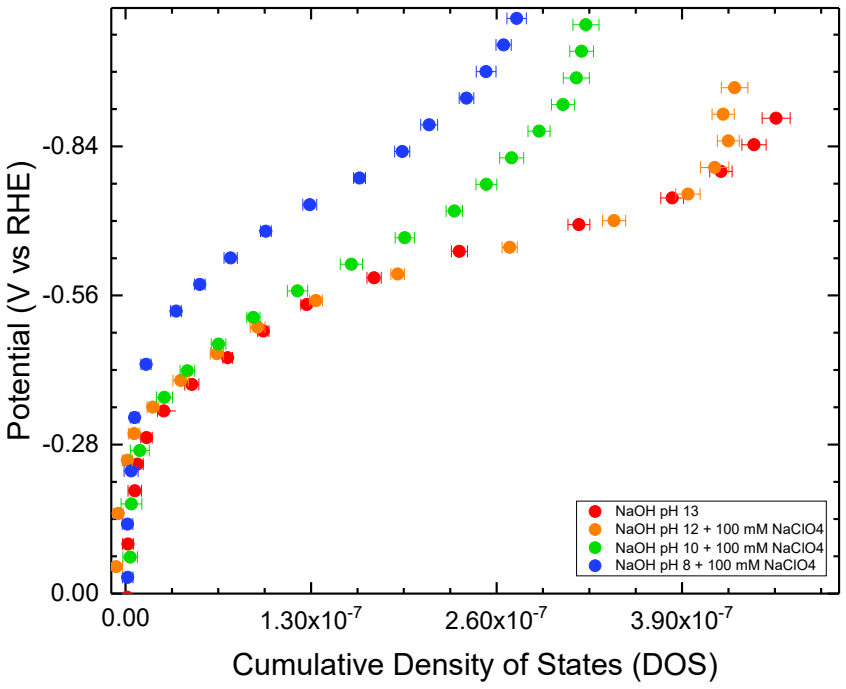

Figure 3.2. Band bending in titanium dioxide films immersed in sodium hydroxide solutions of varying pH. Potential versus the reversible hydrogen electrode (RHE).

vs the potential of the reversible hydrogen electrode (RHE). As seen in **Figure 2**, at potentials more positive than -0.35 V *vs* RHE the density of states near the conduction band edge are nearly pH independent. However, at potential biases more negative than -0.35 V *vs* RHE the pH 8 solution is the only case where the density of states is potentially determined by protons. For pH values of 10, 12, and 13 they are potentially determined by the activity of OH^-. Moreover, in the case of potential determination by H^+, to achieve the same density of states as those where the potential is determined by hydroxide ions requires a greater bias.

Despite some differences in the ability to charge the TiO_2, as observed by differences in the DOS at a given potential step no difference was observed for the post-charging relaxation of the TiO_2 in the various solutions tested. Thus, the discharging processes are likely the same and not governed by the pH, potential determining ions, or the regime of electron concentrations injected in these experiments.

Conclusions

Spectroelectrochemical analysis of the density of states in thin films of nanocrystalline TiO_2 suggest that H_2 evolution limits the ability to populate large concentrations of electrons at large negative applied bias. Data are consistent with solvated protons being the main potential-determining ion in more acidic solutions (pH <= 8) while hydroxide ions are the main potential-determining ion under more alkaline conditions (pH >= 10). These data suggest that to increase the effective charge on each TiO_2 particle, more alkaline aqueous electrolytes are needed to avoid substantial evolution H_2. Further, increasing the charge on a particle as illustrated by the increase of density of states appears to have no effect on the overall kinetics of discharging.

Acknowledgements

We would like to thank Zejie Chen for assistance with some of the spectroelectrochemical experiments whose data is reported in this chapter, as well as undergraduate student researcher Anni Zhang who helped to advance the MATLAB scripts and performed several series of spectroelectrochemical experiments, and undergraduate student researcher Sabina Sebastian for performing initial experiments.

References

(1) Weber, A. Z.; Mench, M. M.; Meyers, J. P.; Ross, P. N.; Gostick, J. T.; Liu, Q. Redox Flow Batteries: A Review. *J. Appl. Electrochem.* **2011**, *41* (10), 1137–1164. https://doi.org/10.1007/s10800-011-0348-2.

(2) Mubeen, S.; Jun, Y. S.; Lee, J.; McFarland, E. W. Solid Suspension Flow Batteries Using Earth Abundant Materials. *ACS Appl. Mater. Interfaces* **2016**, *8* (3), 1759–1765. https://doi.org/10.1021/acsami.5b09515.

(3) Ardo, S.; Meyer, G. J. Photodriven Heterogeneous Charge Transfer with Transition-Metal Compounds Anchored to TiO2 Semiconductor Surfaces. *Chem. Soc. Rev.* **2009**, *38* (1), 115–164. https://doi.org/10.1039/b804321n.

(4) Ito, S.; Murakami, T. N.; Comte, P.; Liska, P.; Grätzel, C.; Nazeeruddin, M. K.; Grätzel, M. Fabrication of Thin Film Dye Sensitized Solar Cells with Solar to Electric Power Conversion Efficiency over 10%. *Thin Solid Films* **2008**, *516* (14), 4613–4619. https://doi.org/10.1016/j.tsf.2007.05.090.

Supplementary Information

Spectroelectrochemical Background

The absorbance of TiO_2 at 800 nm can be modeled by

$$A_{800\,nm} = A^{\circ}_{800\,nm} \cdot e^{-kV} \tag{S3.1}$$

where, $A_{800\ nm}$, is the corrected non-difference absorbance spectra of the TiO_2; $A°_{800\ nm}$, is a constant of absorbance at no bias (V-V_0); k, is a constant of potential; and V, is the potential. Taking the absolute value of the derivative of both sides of **Equation S3.1** results in the instantaneous absorbance, which corresponds to the difference absorbance seen in

$$dA_{800\,nm} = A^{\circ}_{800\,nm} \cdot k \cdot e^{-kV} \tag{S3.2}$$

The difference absorbance is related to the concentration of electrons in the conduction band by the Beer–Lambert law. As Beer–Lambert law is a function of volume, there exists an equivalent analog form that is a function of surface area given by

$$A_{800\,nm} = \varepsilon_{800\,nm} \cdot c \cdot l = 1000 \cdot \varepsilon_{800\,nm} \cdot \Gamma \tag{S3.3}$$

where, $A_{800\ nm}$, is the corrected difference absorbance of the titanium dioxide at 800 nm; $\varepsilon_{800\ nm}$, is the molar extinction coefficient of the electrons in titanium dioxide at 800 nm; c, is the concentration of the species in the volume; l, is the path length of incident light through the sample; Γ, is the moles of electrons per unit area. The 1000 multiplier value comes from accounting for the roughness of the titanium dioxide. Rearrange of **Equation S3.3** and solving gamma in terms of the delta absorbance yields

$$\Gamma = \frac{A_{800\,nm}}{1000 \cdot \varepsilon_{800\,nm}} = \frac{A^{\circ}_{800\,nm}}{1000 \cdot \varepsilon_{800\,nm}} \cdot k \cdot e^{-kV} \quad \text{(S3.4)}$$

Alternatively, solving for the potential yields

$$V = f(\Gamma) = -k \cdot ln \frac{1000 \cdot \varepsilon_{800\,nm} \cdot \Gamma}{A^{\circ}_{800\,nm}} \quad \text{(S3.5)}$$

where, *V*, the potential that the titanium dioxide is held at; *f(Γ)*, is some function of the surface area coverage; i.e. the density of states. The results in this work utilized unfitted absorbance data to report *Γ* and V